Geophysical Journal International

Royal Astronomical Society

Geophys. J. Int. (2024) 236, 1234–1245 Advance Access publication 2023 December 18 GJI Geomagnetism and Electromagnetism https://doi.org/10.1093/gji/ggad477

The effect of heterogeneous contact impedances on complex resistivity measurements

E. Zimmermann¹ and J.A. Huisman²

¹ZEA-2 Electronic Systems, Forschungszentrum Jülich Gmbh, 52428 Jülich, Germany. E-mail: e.zimmermann@fz-juelich.de ²IBG-3 Agrosphere, Forschungszentrum Jülich Gmbh, 52428 Jülich, Germany

Accepted 2023 December 8. Received 2023 December 6; in original form 2023 February 15

SUMMARY

Spectral induced polarization (SIP) and electrical impedance tomography (EIT) are advanced approaches for structural characterisation of soils and rocks based on measurements of the frequency-dependent complex electrical resistivity. Accurate SIP and EIT measurements require the reduction of electrode effects, which have often been attributed to the polarization of metal electrodes in the current pathway. In this study, we demonstrate an alternative electrode effect that influences the accuracy of complex impedance measurements. This alternative electrode effect is caused by a heterogeneous distribution of the contact impedance, which can occur due to ageing or corrosion of the electrode. First, theoretical considerations are given to explain how this electrode effect influences the accuracy of complex impedance measurements. Next, we demonstrate using SIP and EIT measurements that this alternative mechanism better explains the observed electrode effects than previous explanations based only on the presence of metal. The SIP measurements were made on a water-filled container with a metal sphere between two non-polarizing electrodes, which showed that the mere presence of metal in the current pathway only leads to small electrode effects that are typically well below 1 mrad even for small electrode spacings. When the same metal sphere was used as a potential electrode, the observed electrode effect was about 2.5 times larger and varied with rotation. These changes can be explained by a heterogeneous contact impedance resulting in a varying electrode voltage. The EIT measurements were performed with a cylindrical sample holder filled with water. They are used to illustrate how the presented theoretical considerations can be used to investigate the magnitude of the electrode effects for different electrode configurations. We conclude that electrode effects are important to consider for laboratory SIP and EIT measurements and field measurement with closely spaced electrodes.

Key words: Electrical properties; Electrical resistivity tomography (ERT); Image processing; Numerical approximations and analysis; Hydrogeophysics.

1 INTRODUCTION

Complex electrical resistivity measurements in the mHz to kHz frequency range are of increasing interest in hydrogeology, contaminant hydrology, and agricultural engineering (e.g. Kemna *et al.* 2012; Revil *et al.* 2012, 2020; Binley *et al.* 2016). The real part of the complex electrical resistivity of porous media is determined by ionic conduction in the water-filled pore space. In the absence of metal, the imaginary part of the complex electrical resistivity is determined by polarization processes associated with the electrical double layer at the interface between the solid matrix and the pore fluid (e.g. Leroy *et al.* 2008). In the past decade, complex resistivity measurements were shown to be useful in a wide range of applications, including the characterization and monitoring of contaminated sites

(e.g. Flores Orozco *et al.* 2012; Wainwright *et al.* 2016), monitoring and laboratory-scale work of geochemical changes associated with CO₂ injection (e.g. Doetsch *et al.* 2015; Börner *et al.* 2017) as well as biogeochemical processes (e.g. Mellage *et al.* 2018; Zhang & Furman 2022), and the functional characterization of crop root systems (e.g. Weigand & Kemna 2019) amongst other applications.

Different measurement strategies are available to obtain the complex electrical resistivity of soils, sediments and rocks. In the case of time-domain induced polarization measurements, a current is injected into the subsurface using two electrodes, and the resulting voltage decay after shutting of the current is measured at two other electrodes. This approach has been used in laboratory investigations (e.g. Titov *et al.* 2002, 2004), and is widely used for induced polarization measurements in the field (e.g. Doetsch *et al.* 2015;

Olsson et al. 2016; Wainwright et al. 2016; Levy et al. 2022). In frequency-domain induced polarization measurements, a series of sinusoidal excitation signals with a given frequency are injected, and the amplitude and phase of the resulting voltages are measured. Most laboratory studies rely on frequency-domain measurements in the mHz to kHz frequency range and are then commonly referred to as spectral induced polarization (SIP) measurements (e.g. Binley et al. 2005; Leroy et al. 2008; Schmutz et al. 2010; Revil & Florsch 2010; Schwartz & Furman 2012; Izumoto et al. 2020,to name just a few examples). Field systems for frequency-domain IP measurements have also been used, and we call this spectral electrical impedance tomography (sEIT) measurements (e.g. Kemna et al. 2000; Flores Orozco et al. 2011, 2012; Kelter et al. 2018). Independent of the measurement strategy, a high measurement accuracy is required because of the low polarizability of subsurface materials (in the absence of electronically conductive minerals) with typical phase shift values between 0.1 and 20 mrad only (e.g. Binley et al. 2005; Scott & Barker 2005). In the following, we will focus on frequency-domain measurements, but the presented results and implications equally apply to time-domain measurements given the fundamental equivalence between the time and frequency domain.

An important prerequisite for accurate SIP and EIT measurements is that metal electrodes should be moved out of the current path to avoid electrode effects (see e.g. Vinegar & Waxman 1984). This has been well recognized in many laboratory SIP measurement set-ups that have relied on the use of non-polarizing electrodes for voltage measurements (e.g. Ulrich & Slater 2004; Breede et al. 2011). Kelter et al. (2018) compared metal and non-polarizing electrodes for surface EIT measurements, and found that non-polarizing electrodes provided more consistent complex impedance measurements. Although it has been argued that the main reason for using non-polarizing electrodes is to avoid metal in the current pathway, there is little evidence to support this. Considering previous work on the electrical polarization of metal in porous media (Wong 1979; Böcker et al. 2018; Gurin et al. 2019), it seems unlikely that the small volume fraction of metal associated with the electrodes can have a substantial effect on the measured complex electrical resistivity.

In this study, we introduce an alternative mechanism for electrode effects that is associated with a heterogeneous distribution of the contact impedance at the potential electrode surface. For typical measurements, it must be assumed that the surface of the electrode changes with time. This change is caused, for example, by corrosion of non-noble metals (Jöttner & Lorenz 1989). It has also been observed for electrodes made of noble metals if current flows through the electrode (Doering et al. 2022). In typical EIT measurements, effects of both passive corrosion and ageing due to current flow can occur if the potential electrodes are also used for current injection. The effect causes not only a deterioration of the surface structure, but also the deterioration of the homogeneity of the surface. We argue that the importance of heterogeneous contact impedances has previously not been properly recognized. The remainder of the paper is organized as follows. We will first present our theoretical considerations about the effect of heterogeneous contact impedances of potential electrodes on the accuracy of complex impedance measurements. Next, we will provide experimental evidence that the mere presence of metal in the current pathway only leads to small phase measurement errors that are typically well below 1 mrad, but that heterogeneous contact impedances of potential electrodes may lead to more substantial errors. The impact of heterogeneous contact impedances of potential electrodes on electrical imaging results and strategies to reduce this electrode effect will also be

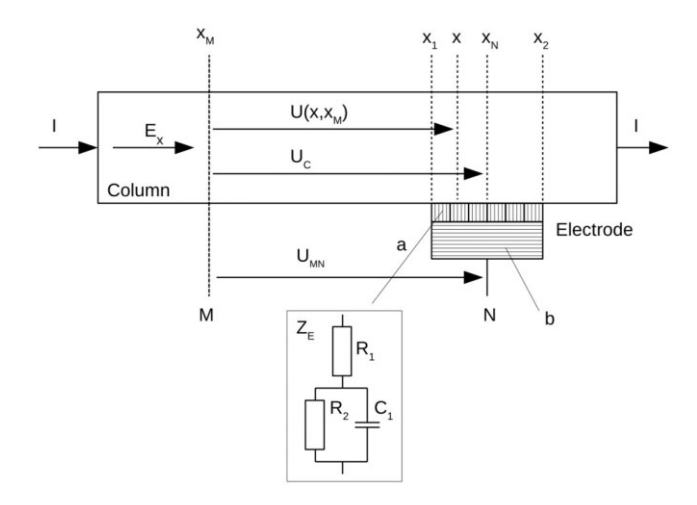


Figure 1. Model for calculating the magnitude and phase error for a measurement with an electrode with heterogeneous contact impedance. The heterogeneous contact between the electrode and sample is described with a simple model for corrosion processes (shown in inset).

discussed. We conclude with a discussion of the implications of this new type of electrode effect for accurate laboratory SIP and field EIT measurements.

2 MODEL CONSIDERATIONS FOR HETEROGENEOUS ELECTRODE SURFACES

Consider a metal potential electrode inserted into a potential field. The electrode potential is measured with a high impedance voltmeter that avoids current flow from the electrode to the voltmeter. In these conditions, the potential inside the electrode adjusts itself such that the sum of the currents flowing through the surface is zero. Because of the very high electrical conductivity of metal, the electric potential is the same everywhere inside this metal electrode. However, different electric potentials may be present at the surface of potential electrodes because of the presence of a contact impedance layer. Therefore, the potential inside the electrode (i.e. the measured potential) depends on the electrode geometry, the potential field distribution around the electrode and the distribution of contact impedances at the electrode surface.

The contact impedance, which describes the electrical transition from ionic conduction to electronic conduction at the electrode surface, is known to cause a frequency-dependent phase shift (Barsoukov & MacDonald 2005). The electrode surface with contact impedances can be represented by a distributed electrical network with frequency-dependent impedances. These frequency-dependent impedances will cause a change of the potential inside the electrode and frequency-dependent amplitude and phase changes in the measured impedance spectrum. In practice, it must be assumed that the electrode surface changes with time and likely becomes more heterogeneous (e.g. due to corrosion), which in turn will lead to increasingly larger phase shifts.

To model the electrode effect associated with heterogeneous contact impedances, the simple 1-D model presented in Fig. 1 will be used. The electrode consists of a heterogeneous contact layer a and a solid electrode metal b. At this point, only one potential electrode is considered to explain the effect of heterogeneous contact impedances. In a next step, the considerations are extended to typical SIP and EIT measurements that rely on two potential electrodes.

In this model, the current I is injected at both ends of the sample, which results in a constant electric field E_x and a position-dependent voltage

$$U(x, x_M) = \int_{x_M}^{x} \vec{E}_x(s) \, ds, \tag{1}$$

between the reference point x_M and the variable position x. If it is assumed that the electric field is parallel to the electrode surface, the calculation of the voltage can be simplified to

$$U(x, x_M) = (x - x_M)E_x. \tag{2}$$

In the ideal case of homogeneous contact impedances, the voltage U_{MN} between the contacts M and N is the nominal voltage

$$U_C = (x_N - x_M)E_x, (3)$$

where $x_N = (x_1 + x_2)/2$ is the middle of electrode N. This nominal voltage U_C can also be used as a reference to calculate the position-dependent voltage

$$U(x, x_M) = \frac{x - x_M}{x_N - x_M} U_C. \tag{4}$$

It is important to note that the deformation of the electrical field E_x due to the presence of the electrode is not considered in this model.

To model the frequency-dependent impedances of the heterogeneous contact layer, a simple model for corrosion processes is used (Jöttner & Lorenz 1989). The model corresponds to the well-known Randles circuit model (Randles 1947) in which the Warburg impedance is neglected. The components of this equivalent circuit model Z_E in Fig. 1 are the resistance R_1 , which represents the ohmic electrolyte resistance (respectively the impedance of the soil), the resistance R_2 , which represents the charge-transfer processes and the capacitance C_1 , which is the capacitance of the electrical double layer at the electrode interface. To simulate a scenario where the effect of an heterogeneous electrode surface has a strong impact, it is assumed that the impedance values of the contact layer have their minimum and maximum on opposite sides x_1 and x_2 of the electrode. It is further assumed that the inverse of $R_2(x)$ [i.e. $G_2(x)$] changes linearly between these two points,

$$G_2(x) = \frac{1}{R_2(x)} = G_{2,\min} + (G_{2,\max} - G_{2,\min}) \frac{x - x_1}{x_2 - x_1},\tag{5}$$

where $G_{2, \min}$ and $G_{2, \max}$ are the minimum and maximum values of G_2 at the electrode sides x_1 and x_2 . The specific quantity R_1 , C_1 and $G_2(x)$ are now used to calculate the position-dependent admittivity

$$Y_E'(x,f) = \frac{1}{R_1 + \frac{1}{G_2(x) + j2\pi fC_1}} \frac{1}{x_2 - x_1}$$
 (6)

(with the unit S m⁻¹) of the contact layer a where f is the measurement frequency. With this admittivity, the current density (with the unit A m⁻¹) across layer a can be calculated using

$$J(x) = (U(x, x_M) - U_{NM}(f))Y_F'(x, f).$$
(7)

In the case that no electrical current flows across contact N in Fig. 1, the integral value of J(x) is zero,

$$\int_{x_1}^{x_2} J(x) \, dx = 0,\tag{8}$$

and the voltage between the electrode contacts \boldsymbol{M} and \boldsymbol{N} can be calculated with

$$U_{MN}(f) = \frac{\int_{x_1}^{x_2} U(x, x_M) Y_E'(x, f) \, dx}{\int_{x_1}^{x_2} Y_E'(x, f) \, dx}.$$
 (9)

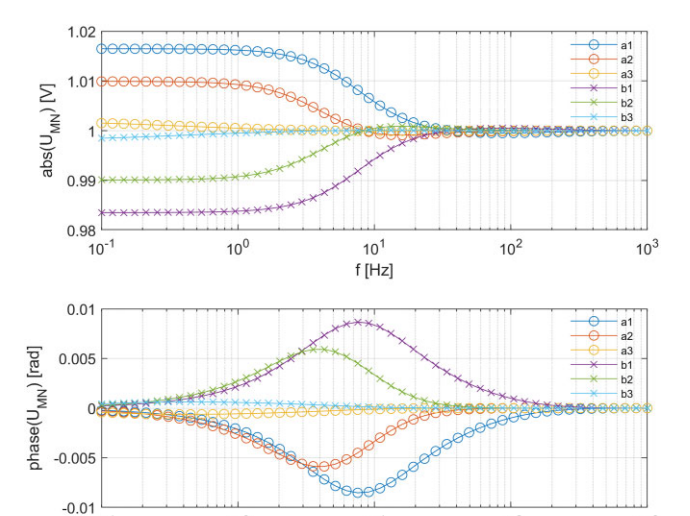


Figure 2. Calculated magnitude and phase spectra of the simulated voltage U_{MN} corresponding to the model in Fig. 1 using $x_M=0$ cm, $x_1=9.5$ cm, $x_2=10.5$ cm, $U_C=1.00$ V, $R_1=[100,3000,100\,000]$ Ω , marked with 1, 2, 3 in the figure legend, $G_{2,\,\rm min}=0$, $G_{2,\,\rm max}=1/(1000\,\Omega)$ and $G_{1}=10\times 10^{-6}$ F. The simulations marked with (a) in the figure legend correspond to an increasing conductance G_2 in x-direction and the simulations marked with (b) correspond with a decreasing conductance G_2 .

f [Hz]

102

10

10-1

10⁰

For the case of a homogeneous contact impedance where $Y'_E(x, f)$ is independent of x, eq. (9) simplifies to

$$U_{MN} = \frac{\int_{x_1}^{x_2} U(x, x_M) \, dx}{\int_{x_1}^{x_2} dx} = U_C. \tag{10}$$

In this case, the predicted amplitude and phase are not frequency dependent.

To illustrate the proposed model, the voltage $U_{MN}(f)$ was calculated as a function of frequency for an electrode diameter of 1 cm, a separation between M and N of 10 cm (i.e. $x_M = 0$ cm, $x_1 = 0$ 9.5 cm, $x_2 = 10.5$ cm) and a nominal voltage $U_C = 1.0$ V. For the parametrization of R_1 , G_2 and C_2 , we assume an electrode area of 1 cm². The resistance R_1 is calculated for a soil cube with a resistivity of 100 Ω m, a length of 1 cm and an area of 1 cm². This results in a resistance of 10 k Ω for this cube. To investigate the effect of R_1 for a larger range of resistivity and effective lengths of the cube, we use R_1 values of 100, 3000 and 100 000 Ω . The values for G_2 and C_2 are taken from (Jöttner & Lorenz 1989) for corroding iron, which are in the mS cm⁻² and μ F cm⁻² range. It is assumed that C_2 does not change quickly due to the corrosion and is therefore assumed to be location-independent in the model. The heterogeneity of the contact impedance due to corrosion is therefore only described by the resistance G_2 . We used $G_{2, \min} = 0$, $G_{2, \max} = 1/(1000 \Omega)$ and C_1 = 10e-6 F.

Two cases were considered where the conductance G_2 either increased or decreased linearly from x_1 to x_2 (Fig. 2). It was found that the magnitude of U_{MN} decreases or increases with frequency depending on whether the conductance G_2 increases or decreases from position x_1 to x_2 . In the low frequency range f_{\min} , the magnitude of U_{MN} varied between 0.984 and 1.016 V. The largest difference between the two cases was obtained for small R_1 value. In the high frequency range f_{\max} , the variation of the voltage was small as expected, because the capacitance was assumed to be independent of position and its admittance is much larger than the conductance

 G_2 . The relative magnitude variation

$$F_V = |\frac{U(f_{\min}) - U(f_{\max})}{U(f_{\max})}|$$
 (11)

between low and high frequencies are $F_V = 1.6$, 1.0 and 0.16 per cent for $R_1 = 100$, 3000 and 100 000 Ω .

This synthetic example clearly shows the effects of a heterogeneous contact impedance when a voltage is applied along the electrode surface. In this example, only R_2 was varied as a function of x. However, it is also possible that C_2 varies as a function of x, which would lead to additional effects of the heterogeneous contact impedances.

To estimate the maximum error of this electrode effect, the maximum voltage variation is calculated, which must lie between the voltages $U(x_1, x_M)$ and $U(x_2, x_M)$ at the two sides of the electrode N. This maximum voltage variation is affected only by the geometry of the electrode N and the electrical field E_x at the electrode, and can be calculated as

$$U_{V\max,N} = U(x_2, x_M) - U(x_1, x_M) = (x_2 - x_1)E_x$$

= $(x_2 - x_1)\frac{U_C}{x_N - x_M}$, (12)

using eq. (3) and (4) where the electrical field can be calculated from the nominal voltage U_C and the geometry of the sample for this simple setup. To obtain the relative magnitude variation, eq. (12) is normalized by the voltage U_C :

$$F_{V\max,N} = \left| \frac{U_{V\max,N}}{U_C} \right| = \left| \frac{x_2 - x_1}{x_N - x_M} \right| \tag{13}$$

So far, a single electrode has been analysed. However, SIP and EIT measurements are typically made between two electrodes. The maximum voltage variation of the second electrode can be obtained using

$$U_{V_{\max,M}} = U(x_2', x_N) - U(x_1', x_N) = (x_2' - x_1')E_x$$

= $(x_2' - x_1')\frac{U_C}{x_N - x_M}$, (14)

where x_1' and x_2' are the left and right boundaries of the second electrode. To estimate the maximum voltage variation for measurements between two potential electrodes with similar type of construction, the root square sum of the voltage variation $U_{V\max,N}$ and $U_{V\max,M}$ of the electrodes N and M is calculated:

$$U_{V\max} = \sqrt{U_{V\max,N}^2 + U_{V\max,M}^2} \tag{15}$$

Here, it is assumed that the individual voltages variations at the electrodes are statistically independent of each other. This is plausible given that the generation of identical distributions of heterogeneous contact impedances at the surface of two electrodes by an external process is difficult to imagine. Similar to eq. (13), the maximum relative magnitude variation between two electrodes is obtained using

$$F_{V\max} = \left| \frac{U_{V\max}}{U_C} \right| \tag{16}$$

This ratio is the maximum relative magnitude variation that can occur given the geometry of the electrode. In the simulations presented in Fig. 2, the distance between the electrodes N and M is 10 cm and the distances between the electrode boundaries x_2 and x_1 is 1 cm. This results in a maximum relative magnitude variation of $F_{V_{\max},N}=0.1$ if only one electrode is considered. The highest simulated relative magnitude variation obtained from Fig. 2 is $F_V=1.6$ per cent, which is considerable lower than $F_{V_{\max},N}$. It is

therefore desirable to obtain a relationship between the maximum relative magnitude variation and a realistic variation that occurs with typical EIT measurements, which will be discussed next.

From the considerations presented above, it is clear that the expected magnitude variation depends on the geometry of the sample and the electrode and the frequency-dependent behaviour of the contact impedances. Normally, the behaviour of the contact impedances is not known, especially if electrodes are in use for a longer time. Therefore, the magnitude variation was estimated from geometrical considerations only. For this, weighting factors are introduced that allow the estimation of possible electrode effects in terms of magnitude variation and phase error. It is assumed that these weighting factors are independent of the geometry and can thus be used to roughly estimate electrode errors. To obtain a estimate of the magnitude variation, the following relationship was defined:

$$F_V = W_V \times F_{V \text{max}} \tag{17}$$

where W_V is the weighting factor for the magnitude. For the results presented in Fig. 2, the weighting factors $W_V = 0.16$, 0.10 and 0.02 are obtained. The weighting factor W_V will later be calculated for actual impedance measurements as well.

In addition to the relative magnitude variation, the phase variation is especially important for the evaluation of the measurement accuracy of SIP and EIT measurements. Since the model in Fig. 1 uses a linear time-invariant electrical network, the phase response is directly related to the frequency-dependent changes in the magnitude of U_{MN} . Depending on the direction of the magnitude variation, the simulated phase is positive or negative. However, the phase variation also depend on the shape of the amplitude curve according to the Kramers–Kronig relationships. Since we do not know the heterogeneity of the contact impedances in real measurements, it is not possible to model the shape of the amplitude curve or the phase spectrum. To nevertheless obtain an estimate for the phase variation, a further weighting factor is introduced:

$$F_P = W_P \times F_V = W_P \times W_V \times F_{V\text{max}} \tag{18}$$

where W_P is the weighting factor for the estimation of the phase variation. This factor is determined independently of W_V from the magnitude variation and the phase of typical measurements and also depends only on the heterogeneity of the contact impedances. The two factors together should later enable an estimation of the phase error from the geometry data of the electrodes and the system. In case of the simulation results presented in Fig. 2, the value of W_P is 544 mrad for $F_V = 1.6$ per cent and the maximum phase variation (phase peak) of $F_P = 8.7$ mrad.

For the evaluation of the measurement data, we still need a relationship to the measured impedance values. For this, the maximum voltage $U_{V\max}$ and the measured voltage U_{MN} between electrodes M and N are normalized with the exciting current I to obtain the maximum impedance variation

$$Z_{V\max} = \frac{U_{V\max}}{I} \tag{19}$$

and the transfer impedance

$$Z_{MN(f)} = \frac{U_{MN}(f)}{I}. (20)$$

Finally, the relative magnitude variation is calculated using

$$F_V = \frac{\Delta Z_{MN}}{Z_C} \tag{21}$$

where ΔZ_{MN} is determined from the impedance variation at the lowest and highest frequency:

$$\Delta Z_{MN} = |Z_{MN}(f_{\min}) - Z_{MN}(f_{\max})| \tag{22}$$

and the nominal impedance Z_C is determined from the impedance at the highest frequency:

$$Z_C = |Z_{MN}(f_{\text{max}})| \tag{23}$$

This approach is supported by the simulation results presented in Fig. 2, where it can be seen that the largest magnitude variation occurs between the lowest and highest frequency and that the impedance at high frequencies is similar to the nominal impedance $Z_C = U_C/I$.

3 EXPERIMENTAL STUDIES

3.1 SIP and EIT measurement systems

In this study, both SIP and EIT measurements were used to investigate electrode effects on complex impedance measurements. SIP measurements were made using the system presented in Zimmermann et al. (2008a). This system uses a sinusoidal excitation voltage of up to ± 10 V with a known frequency to inject current in the sample. The amount of injected current is measured using a shunt resistor. An amplifier unit measures the voltages at all electrodes relative to ground using triaxial cables with driven shields to connect the electrodes to the amplifiers. The input capacitance between the input of the cable (at the position of the electrode) and ground is 4.7 pF, while the input resistance is 500 G Ω . The measured voltages are digitized using data acquisition cards (NI4472, National Instruments, Austin, TX, USA).

EIT measurements were made using the 40-channel extension of the SIP measurement system described in Zimmermann et al. (2008b, 2010). In addition to the components of the SIP measurement system, this system consists of 40 electrode modules with shielded cables and a multiplexer unit. For each measurement, two electrodes are used for excitation and all other electrodes simultaneously measure the voltages relative to system ground. This enables fast EIT measurements with a free choice of potential electrode pairs during post-processing. To minimize the capacitive load on the electrodes, amplifiers for potential measurement and relays for switching off the inactive current channels are implemented in the electrode modules. The input impedance of the electrode modules consists of an input capacitance of about 10 pF and an input resistance of about 500 G Ω . Several error corrections are made during the subsequent impedance calculation. In particular, correction methods have been developed to remove gain errors, signal drift, current measurement errors and to compensate cable propagation delays. More information about the system design and the methods for error correction can be found in Zimmermann et al. (2010). Additional design considerations for surface EIT applications are discussed in Zimmermann et al. (2019) and Weigand et al. (2022). For both systems, measurements are further processed using custom-made LabView (National Instruments) and Matlab (Mathworks, Natick, MA, USA) programs.

3.2 SIP measurements

In a first experiment, the frequency-dependent impedance of a simple sphere made of stainless steel with a diameter of 8 mm was measured in a rectangular sample holder using the SIP system. The

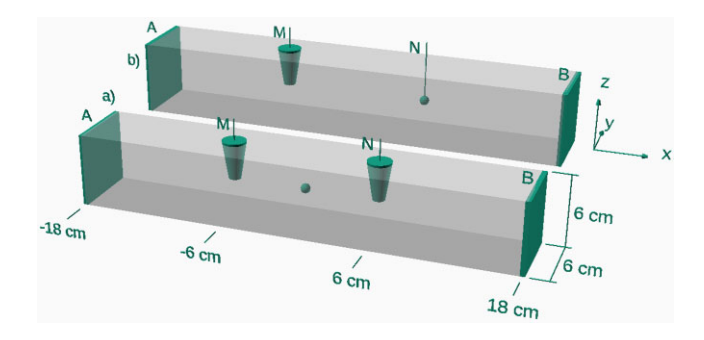


Figure 3. (a) Experimental setup for measuring the SIP response of a polarizable metal sphere between the potential electrodes M and N in the centre of the sample holder. (b) Experimental set-up for measuring the SIP response of the metal sphere as the potential electrode N.

sample holder has a cross-section of $6 \times 6 \text{ cm}^2$ and was filled with water with an electrical resistivity of 28 Ω m. The electrical field was applied perpendicular to the cross-section with plate-shaped current electrodes A and B positioned at -18 and 18 cm (Fig. 3a). The resulting voltages were measured with the electrodes M and N positioned at -6 and at 6 cm. To avoid polarization effects (or effects due to heterogeneous contact impedance) associated with the current electrodes, the distance between the current and potential electrodes was twice the cross-sectional width as recommended by Zimmermann et al. (2008a). To avoid polarization effects (or effects due to heterogeneous contact impedance) for the potential electrodes, porous water-filled hollow ceramic cones with low contact impedance (average diameter = 12 mm, active length = 30 mm) were used for the electrical contact with the sample, using the same water as in the sample holder. This potential electrode design was similar to designs used in previous studies (Ulrich & Slater 2004; Zimmermann et al. 2008a; Breede et al. 2011). Using this measurement set-up, any measured phase can be attributed to the presence of the metallic sphere.

In a second experiment, the described sphere was used as potential electrode N (Fig. 3b). The potential electrode M was not changed. Impedance spectra were measured twice using this setup. The only difference between the two measurements was that the metal sphere used as potential electrode was rotated around the z-axis by 180° . The sphere was not cleaned prior to the measurements and may thus have an heterogeneous contact impedance at the surface.

3.3 EIT measurements

To investigate electrode effects in tomographic measurements, EIT measurements were made in controlled conditions. For this, a cylindrical sample holder with a diameter of 190 mm filled with water with an electrical resistivity of 22 Ωm and a water height of 40 mm was used (Fig. 4a). The sample holder was equipped with 16 brass electrodes with a diameter of 6 mm, which were used for current injection and voltage measurements. The electrodes were symmetrically arranged around the column at a height of 20 mm from the inner bottom and they were numbered sequentially from 1 to 16. Electrodes with even numbers were retracted by 14 mm from the inner boundary of the container inside electrode chambers (plastic cable glands with inner diameter 7 mm) to avoid electrode effects. The electrodes with odd numbers were placed with the end of the metal plane to the inner boundary (Fig. 4b). To avoid polarization (or

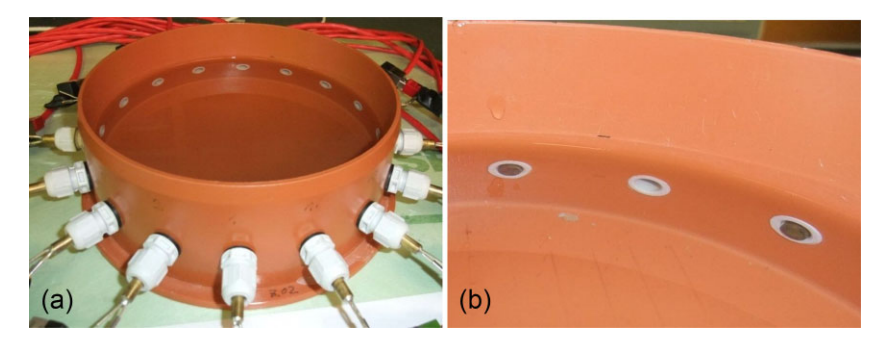


Figure 4. (a) Experimental set-up to investigate electrode effects in EIT measurements. (b) Close-up showing retracted and non-retracted electrodes at the inner boundary of the column.

effects due to heterogeneous contact impedance) of the current electrodes, the current is only injected at the retracted electrodes with even numbers using a skip-five electrode procedure (2–8, 8–14, ...) and voltages were measured at all other electrodes. To analyse these measurements, two different sets of four-electrode configurations will be considered. In the first set, only retracted metal electrodes are considered as potential electrodes. In this case, the non-retracted (plane) electrodes only act as metal objects that potentially distort the measurements. In the second set of measurements, voltages are measured at the non-retracted electrodes. It is important to emphasize that the electrodes were not cleaned prior to the following tests, and may thus have an heterogeneous contact impedance at the electrode surface.

To demonstrate the effect of electrode effects on EIT imaging results, the two sets of EIT measurements obtained with non-retracted and optimally retracted electrodes were inverted to obtain the 2-D complex resistivity distribution at the height of the electrodes. For the inversion, the transfer impedances were modelled with a 3-D FEM model with tetrahedral elements using a custom-made Matlab program (Zimmermann 2011). The electrodes are considered as point electrodes on the inner side wall of the container. A Gauss-Newton procedure with generalized Tikhonov regularization was used. For regularization, a second order smoothing filter was applied to the 2-D plane. To determine the optimum setting of the regularization parameter, the L-curve approach was used (Hansen et al. 2007). Data weighting was not used and all measured transfer impedances were equally weighted in the inversion.

4 RESULTS AND DISCUSSION

4.1 SIP measurements with metal sphere

Fig. 5 shows the measured impedance for a metal sphere with a diameter of 8 mm between the potential electrodes using the set-up shown in Fig. 3(a). In the absence of the metal sphere, the measured impedance magnitude for water is expected to be independent of frequency and the phase is expected to be close to zero. It can be seen that the measured impedance magnitude ranged from 917.0 to 913.5 Ω in the presence of the metal sphere. This corresponds to a relative magnitude variation of $F_V = 0.37$ per cent. The associated phase variation is $F_P = 0.8$ mrad measured at 10 Hz. These relatively low magnitude and phase variations are related to the volume fraction of the metal, which is only 0.0006 (relative to the volume of water between the potential electrodes). With increasing electrode spacing, the relative volume fraction and thus the expected phase shift becomes even smaller, as can also be seen from the modelling work of Böcker *et al.* (2018).

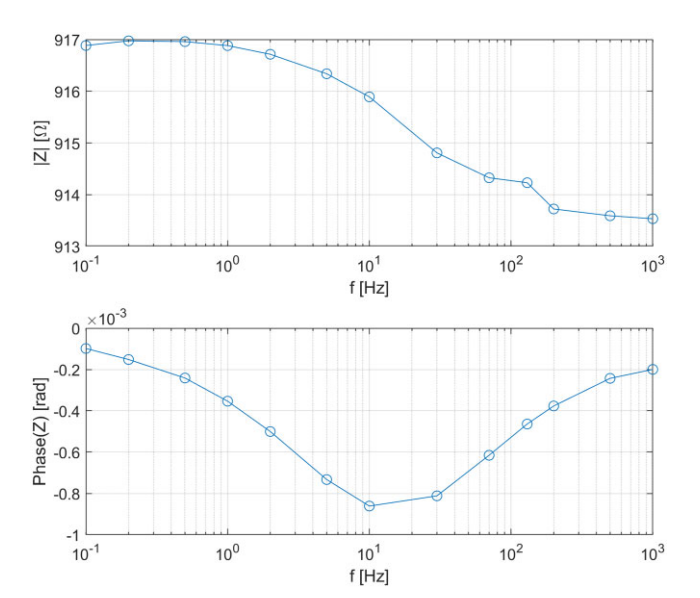


Figure 5. Measured magnitude and phase of the impedance for a metal sphere with a diameter of 8 mm using the set-up shown in Fig. 3(a).

Fig. 6 shows the measured complex impedance when the same metal sphere is used as one of the potential electrodes. Two different measurements are shown and the only difference between them is that the metal sphere was rotated around the z-axis by 180° (left-right). It can be seen that the rotation of the electrode had a significant effect on the measured impedance magnitude and that positive phase values were obtained in one of the measurements. The observed magnitude variation (mean value of both measurements) was $F_V = 0.82$ per cent and the phase variation was $F_P = 2.4$ mrad, which is about 2.5 times larger than the values due to the presence of metal (Fig. 5). These relatively high magnitude variations as well as the observed changes with a rotation of the electrode suggest that the presence of metal alone is not sufficient to explain these measurement results. Instead, we argue that the observed changes can be explained when a varying electrode voltage in the presence of an heterogeneous contact impedance is invoked.

Further analysis of the measured phase shown in Fig. 6 suggests that the ratio of the phase variation to the amplitude variation W_P is 292 mrad. This value is smaller than the value of 544 mrad obtained for the simulation results presented in Fig. 2. This difference is related to the slower change of the impedance magnitude as a function of frequency for the actual measurements, which also implies a lower peak in the phase according to the Kramers–Kronig relationship. Fig. 2 already showed that the phase maximum and the frequency of the phase maximum depend on the value of R_1 .

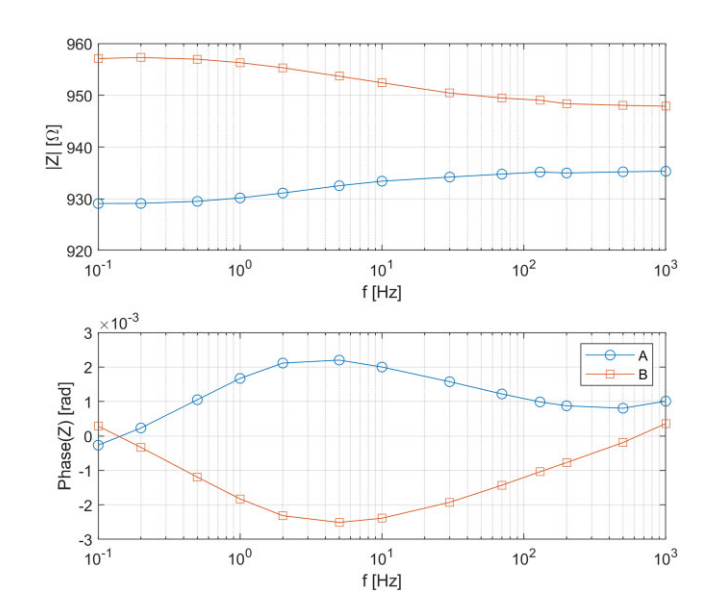


Figure 6. Measured magnitude and phase of the impedance when a metal sphere with a diameter of 8 mm was used as potential electrode using the set-up shown in Fig. 3(b). The only difference between the measurements is a rotation of the sphere by 180° .

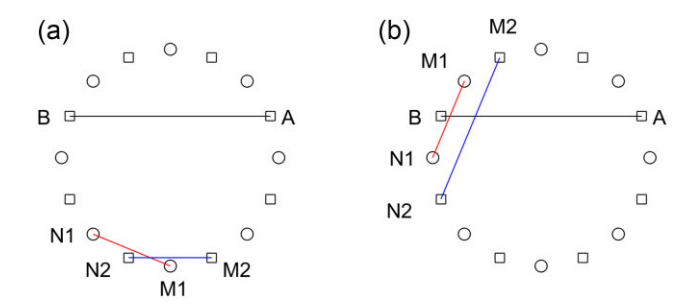


Figure 7. Configuration of the measurements with retracted current electrodes (A and B) and retracted (M2–N2, blue line) and non-retracted (N1–M1, red line) electrodes used to obtain the results presented in (a) Fig. 8 and (b) Fig. 9. The square and circles indicates the retracted and non-retracted electrodes.

In addition, the linear variation of $1/R_2$ along the electrode surface is a strong simplification, and R_2 can vary arbitrarily as a function of position x in reality. Thus, we attribute the slower change of the impedance magnitude observed in the experimental data (Fig. 6) to additional and unknown location-dependent variations not considered in the model.

4.2 EIT measurements with water-filled container

To further investigate electrode effects, EIT measurements were made on the cylindrical water-filled container shown in Fig. 4(a). In these measurements, non-retracted electrodes were either used as polarizable objects between two retracted potential electrodes or directly as potential electrodes. In a first step, all measurements with the relative electrode configurations illustrated in Fig. 7(a) were analysed. Due to the radial symmetry, this resulted in 16 measurements for one current configuration with all associated potential electrode configurations. Fig. 8 presents the magnitude and phase of the measured transfer impedance for these measurements. In the case of the measurements with retracted current and potential electrodes, the magnitude of the measured transfer impedance is very

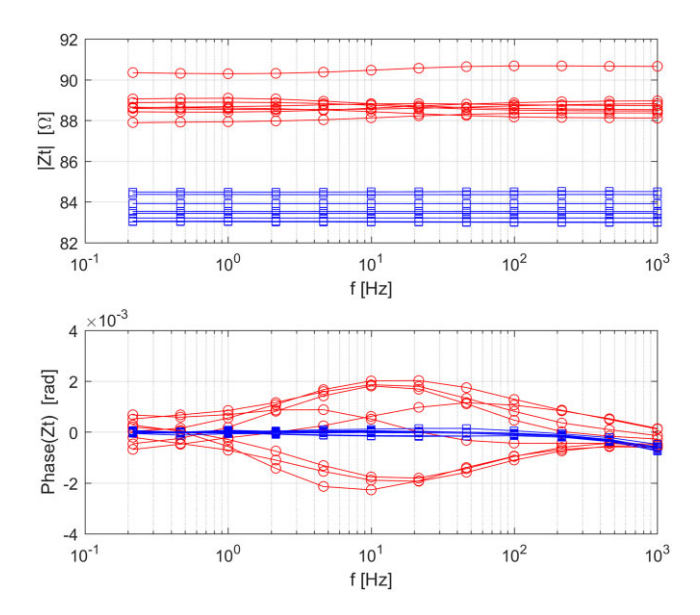


Figure 8. Measured magnitude and phase of impedance with retracted current electrodes and retracted (blue) and non-retracted (red) potential electrodes for the electrode configurations shown in Fig. 7(a).

similar because of the radial symmetry of the sample holder. Furthermore, it can be seen that the phase of these measurements is small and close to zero as expected for a measurement of water. A close inspection of the measurements with retracted electrodes showed a small peak in the measured phase due to the presence of the non-retracted potential electrodes between the retracted electrodes (similar to the case of the SIP measurements shown in Fig. 5). Nevertheless, the maximum magnitude and phase errors were small with $F_V = 0.06$ per cent and $F_P = 0.3$ mrad ($W_P = 500$ mrad). This again confirms that the mere presence of metal only introduces minor errors in the phase measurements. The results for EIT measurements using the same electrodes for current injection but nonretracted electrodes for potential measurements are also presented in Fig. 8 and showed much larger errors. The maximum magnitude and phase error are $F_V = 0.6$ per cent and $F_P = 2$ mrad ($W_P =$ 333 mrad), which is much higher than the maximum magnitude and phase errors of the measurement with the retracted electrodes although both sets of measurements have the same amount of metal in the container.

EIT measurements obtained with the electrode configuration shown in Fig. 7(b) were analysed next. For this configuration, the current electrode B is between the potential electrodes M and N. In this case, the electric field strength across the potential electrode surface and the associated maximum impedance variation Z_{Vmax} is high and the measured nominal impedance Z_C is relatively small. According to the model considerations for the effect of heterogeneous electrode surfaces (eq. 16), this should lead to substantially larger electrode effects in the EIT measurements. Fig. 9 presents the magnitude and phase of the measured transfer impedance for these electrode configurations. It can be seen that the measurements using the non-retracted potential electrodes indeed showed high amplitude and phase errors. The maximum magnitude and phase error are $F_V = 10$ per cent and $F_P = 40$ mrad ($W_P = 400$ mrad). In comparison, the maximum magnitude and phase error using the retracted electrodes are much lower with $F_V = 0.2$ per cent and F_P $= 0.8 \text{ mrad } (W_P = 400 \text{ mrad}).$

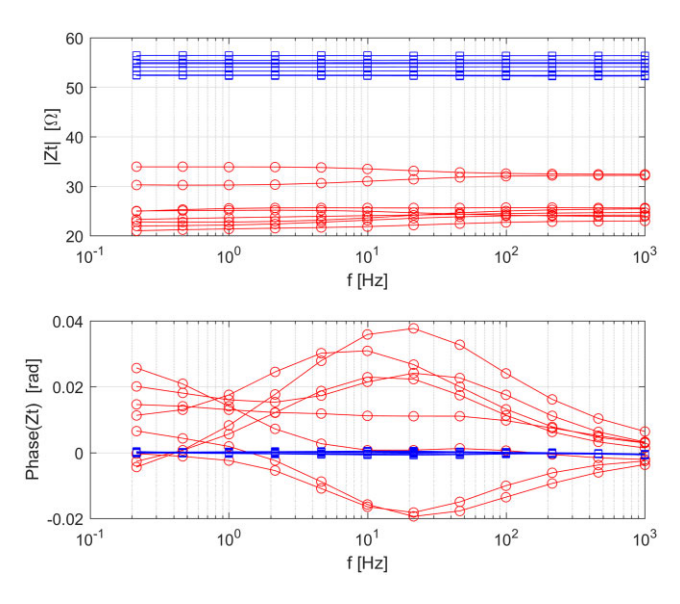


Figure 9. Measured magnitude and phase of impedance with retracted current electrodes and retracted (blue) and non-retracted (red) potential electrodes for the electrode configurations shown in Fig. 7(b).

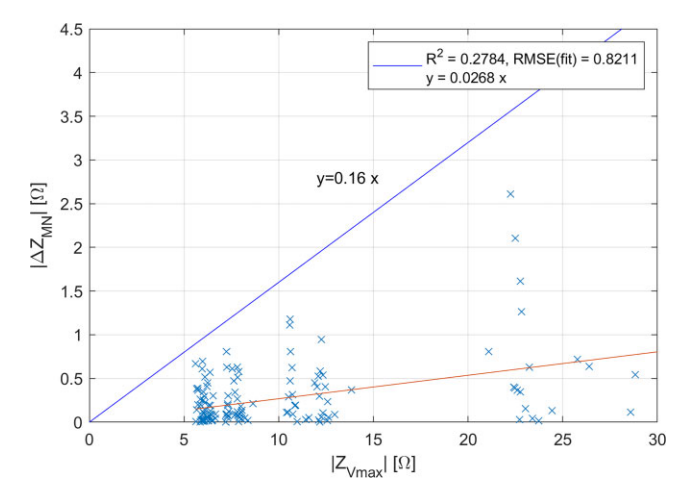


Figure 10. Comparison between the modelled and measured variation of the impedance magnitude variation $Z_{V\max}$ and ΔZ_{MN} . The blue line indicates the expected maximum error using the weighting factor $W_V = 16$ per cent determined from the modelling results presented in Fig. 2. The red line indicates the actual fit between $Z_{V\max}$ and ΔZ_{MN} , which suggests a weighting factor W_V of 2.7 per cent.

In a next step, the applicability of the maximum error estimates obtained with the proposed model are evaluated. For this, the variation of the measured impedance magnitude ΔZ_{MN} obtained with non-retracted potential electrodes was compared with the theoretical maximum magnitude variation $Z_{V\max}$ (Fig. 10). To obtain $Z_{V\max}$, the electric fields at the potential electrodes were calculated using the 3-D FEM model of the sample for similar nominal impedance values Z_C . These simulated electrical fields were used to calculate the voltage across each electrode according to eqs (12) and (14), and the maximum impedance magnitude variation for a pair of potential electrodes was obtained with eqs (15) and (19). As expected, the theoretical maximum magnitude variation was substantially larger than the measured magnitude variation. Some measured values were close to the values obtained using a weighting factor W_V = 16 per cent determined from the modelling results presented in Fig. 2 for $R_1 = 100 \Omega$. However, the average value of the weighting

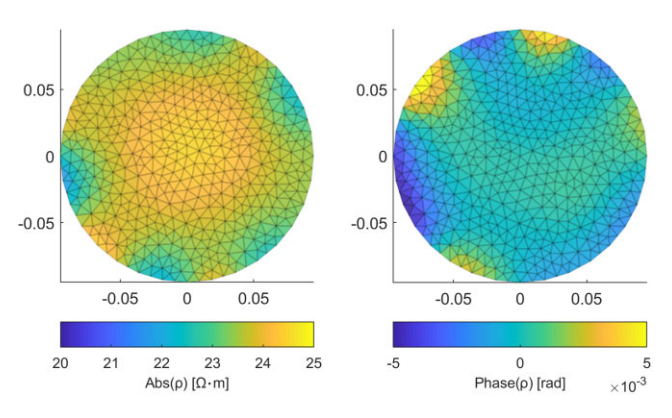


Figure 11. Inverted amplitude and phase of the electrical resistivity at 21 Hz using measured data obtained with non-retracted potential electrodes.

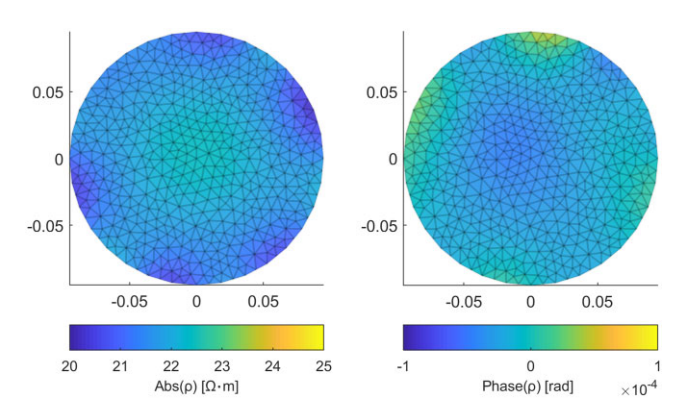


Figure 12. Inverted amplitude and phase of the electrical resistivity at 21 Hz using measured data where all electrodes were retracted by 14 mm.

factor was $W_V = 2.7$ per cent for this EIT data set. For the practical assessment of electrode errors, it therefore does not make sense to start from the extreme values of 16 per cent obtained from the simulations. It seems more reasonable to use the value of $W_V = 2.7$ per cent obtained from the actual measurements.

Based on the simulation and measurement results, an appropriate value W_P for the conversion from amplitude to phase was also determined. The maximum phase change with a pronounced phase peak is obtained when the amplitude change occurs in a small frequency range. For the cases where this occurred, the value of W_P was as high as 500 mrad. In general, the estimated values of W_P varied between 292 and 500 mrad for the EIT data set presented here. Therefore, we will use the conservative estimate of $W_P = 500$ mrad to estimate the phase peak error F_P using eq. (18) in the discussion of the implications for SIP and EIT measurements in the next sections.

In a final step, it is shown how the presented electrode effects affect EIT imaging results. Figs 11 and 12 show the magnitude and phase of the electrical resistivity at 21 Hz for the case that the EIT measurements are performed with non-retracted (plane) (Fig. 11) and optimally retracted potential electrodes (Fig. 12). According to Figs 8 and 9, the phase error was largest at the selected frequency of 21 Hz.

For the inversion, the same electrode configurations as well as regularization factor were used. The comparison shows clear differences in the inverted phase of the resistivity. The deviation from the expected phase of 0 mrad is up to 5 mrad for the non-retracted electrodes, whereas the inverted phase for the retracted electrodes was more than 50 times smaller with deviations mostly below

Table 1. Maximum phase of the measured transfer impedance and the mean impedances between the active current electrodes measured in the range from 1 to 21 Hz.

Depth of retraction	0 mm	5 mm	7 mm	14 mm
$Max[phase(Z_t)]$	80 mrad	9 mrad	1.8 mrad	0.8 mrad
$ Z_{ce} $	$4 \text{ k}\Omega$	$9 \text{ k}\Omega$	$10 \text{ k}\Omega$	$17 \text{ k}\Omega$

0.1 mrad. The minor difference in the resistivity magnitude for the two data sets is attributed to slightly different water levels that were not adequately captured in the forward model.

4.3 Impact on laboratory SIP and EIT measurements

For laboratory SIP and EIT measurements, close proximity of electrodes can often not be avoided and these measurements are thus particularly susceptible to electrode effects. This is already well established, and electrode effects are typically avoided by retracting the electrodes out of the electrical field while maintaining contact with the sample. In the case of saturated samples, this contact can easily be achieved through a liquid-filled bridge. To investigate how much electrodes need to be retracted, we made two sets of additional measurements with the sample holder shown in Fig. 4 using partially retracted electrodes. This resulted in four data sets where the electrodes were variably retracted by 0, 5, 7 and 14 mm. The current was injected with a skip-two electrode procedure (1-4, 4-7, ...) and the voltages were measured at the same electrode pairs except those that include current electrodes. Analysis of these four data sets showed that the maximum phase error in the frequency range from 1 100 Hz decreased quickly with increasing depth of retraction (Table 1). When the electrodes were retracted by 14 mm, the typical spectral shape of the electrode effects (similar to Fig. 8) could not be recognised anymore. The remaining phase error of 0.8 mrad is attributed to other sources of measurement noise. The retraction of electrodes in their electrode chamber resulted in a moderate increase of the contact impedance $|Z_{ce}|$ (absolute value of the complex impedance) of the potential electrodes due to the increased length of the water-filled channel as indicated by the increase in the measured impedance between the current electrodes. This increase in contact impedance will affect the measurement accuracy in the kHz frequency range. However, the observed contact impedance was sufficiently low such that accurate correction using the approach proposed by Huisman et al. (2016) and extended by Wang & Slater (2019) is feasible. Based on these results, we recommend retracting electrodes by at least two times the diameter of the electrode chambers to avoid electrode effects making sure that there is no air in the chambers.

For samples where the liquid bridge between the metal electrode and the sample cannot be maintained (e.g. unsaturated porous media), we recommend the use of an alternative electrode design relying on membranes as in the case of non-polarizing electrodes for self-potential measurements. A possible design consisting of a plastic tube with ceramic tip and a metal wire inside was presented by Breede *et al.* (2011). In this study, a ceramic tip with a high air entry value of 2000 hPa (largest pore size: $0.3~\mu m$) and a contact area of $0.5~cm^2$ was used to minimize fluid exchange between electrode and medium and to ensure a liquid bridge between metal electrode and sample even in dry porous media. It is still essential to retract the metal electrode inside the plastic tube to avoid electrode effects. The disadvantage of this design is the relatively high additional contact impedance associated with the ceramic tip. One strategy to reduce the contact impedance is to use a liquid with

low electrical resistivity inside the tube. However, the unavoidable exchange of ions between the electrode liquid and the sample liquid through advection and diffusion is not desirable for most laboratory applications. Therefore, we recommend to match the resistivity of the liquids in the electrode chambers and the sample. Other strategies to reduce the contact impedance are to increase the surface area of the ceramic tip and to select a ceramic with a lower air-entry pressure. The latter option may lead to premature drainage of the ceramic tip in unsaturated soils (with high suction). This brief discussion shows that the selection of a proper ceramic tip requires a compromise between several factors, and may also depend on the expected experimental conditions.

4.4 Impact on field EIT measurements

The presented results can also be used to make recommendations to avoid electrode effects in field EIT measurements. Obviously, this can be achieved by the use of non-polarizing electrodes, which ensure that the metal electrode is out of the current pathway. However, the use of metal electrodes inserted into the subsurface is much more convenient in many cases.

Since the contact impedance of the electrode is usually not known and will likely change with time, an error estimation can only be made by calculating the maximum relative magnitude variation $F_{V\max}$ from the geometry data of the electrodes and the electrode configuration. For electrode configurations where the electric field is not constant, the well-known half-space solution or FEM modelling can be used to calculate $F_{V\max}$. However, it is simpler in the case of a constant electric field where the relative amplitude variation is approximately the quotient of the electrode diameter d and the electrode distance a:

$$F_V = W_V \times F_{V \text{max}} \approx W_V \frac{\sqrt{2}d}{a}.$$
 (24)

Analogous to eq. (15), we consider the effect of two similar electrodes by calculating the square root of the sum of squares of the two parts, which is accounted for by the factor $\sqrt{2}$. Using these assumptions, the error is $F_V = 0.038$ per cent for electrodes of d = 10 mm at a distance of 1 m using a weighting factor of $W_V = 2.7$ per cent. The maximum phase value for this example is $F_P = 0.19$ mrad when the conservative estimate of $W_P = 500$ mrad is considered.

This error estimation can easily be extended to typical electrode configurations used in the field (e.g. Schlumberger, Wenner and dipole–dipole, see Table 2). First, we describe the error estimation for the Schlumberger configuration (A < na > M < a > N < na > B), where a is the distance between the electrodes and a is an integer factor. For the case that the distance between the current electrodes is significantly larger than the distance between the potential electrodes (a > 1), the electric field at the potential electrodes is almost constant and the geometrical relation according to eq. (24) can be used to estimate the expected error. According to the above calculation, the magnitude and phase error thus is a = 0.038 per cent and a = 0.19 mrad using a = 2.7 per cent, a = 500 mrad, a = 10 mm and a = 1 m. Even for a potential electrode separation as small as 0.25 m, the estimated phase error a is only 0.76 mrad.

When n=1, the Schlumberger configuration simplifies to the Wenner configuration (A < a > M < a > N < a > B) with equal distances between the electrodes. In this case, the current electrodes are closer to the potential electrodes and the assumption of a constant electrical field between the potential electrodes is not valid. Using

and an electrode separation of $a = 1$ m using the weighting factors $W_V = 2.7$ per cent and $W_P = 500$ mrad.								
Configuration		а	n	F_V	F_P			
Schlumberger	(A < na > M < a > N < na > B)	1 m	>>1	0.038 per cent	0.19 mrad			
Schlumberger	(A < na > M < a > N < na > B)	0.25 m	< < 1	0.152 per cent	0.76 mrad			

Table 2. Error estimation for typical field electrode configurations for electrodes with a diameter of d=10 mm

Configuration		а	n	F_V	F_P
Schlumberger	(A < na > M < a > N < na > B)	1 m	>>1	0.038 per cent	0.19 mrad
Schlumberger	(A < na > M < a > N < na > B)	0.25 m	>>1	0.152 per cent	0.76 mrad
Wenner	(A < a > B < a > M < a > N)	1 m	_	0.048 per cent	0.24 mrad
Dipole-dipole	(A < a > B < na > M < a > N)	1 m	1	0.062 per cent	0.31 mrad
Dipole-dipole	(A < a > B < na > M < a > N)	1 m	>>1	0.038 per cent	0.19 mrad
Gamma	(A < a > M < a > B < a > N)	1 m	_	0.089 per cent	0.44 mrad
Gamma	(A < a > M < a > B < a > N)	0.25 m	-	0.350 per cent	1.77 mrad

the well-known solution for the electric potential distribution in a homogeneous half-space, it can be estimated that the electric field at the electrodes is 40 per cent higher compared to the field in the middle between the potential electrodes. Due to the parabolic shape of the electric field strength with a minimum in the middle between the electrodes, the voltage U_C between the potential electrodes is also higher compared to the case with constant field strength. This leads to a 25 per cent higher voltage $U_{V\max}$ in relation to U_{C} and an error F_V which is 1.25 times higher compared to a calculation with a constant electrical field. For a Wenner configuration with d = 10 mm and a = 1 m, the magnitude and phase error thus is $F_V =$ 0.048 per cent and $F_P = 0.24$ mrad with the same assumptions as used previously.

For the dipole-dipole configuration (A < a > B < na > M < a >N), the highest error occurs when the potential electrodes are close to the current electrodes (n = 1). For a dipole-dipole configuration with d = 10 mm, a = 1 m, and n = 1, the magnitude and phase error thus are $F_V = 0.062$ per cent and $F_P = 0.31$ mrad. For very large values of n, the error values are $F_V = 0.038$ per cent and $F_P = 0.19$ mrad for this electrode diameter. Similar to the Wenner configuration, it was found that the error F_V is 1.62 times higher for n = 1 compared to the case of a constant electrical field between the potential electrodes for large values of n.

Gamma configurations (A < >M < >B < >N) are the most critical configurations with respect to electrode effects because of possible low voltage difference U_C between the potential electrodes in the presence of a strong electrical field at the potential electrodes (i.e. as in the measurements presented in Fig. 9). A high voltage variation $U_{V\max}$ at the electrodes in relation to a small voltage U_C between the electrodes can cause extremely large errors F_V and F_P . Therefore, it is difficult to obtain a general estimate for this type of electrode configuration. Nevertheless, the error for any given configuration can be estimated using the half-space solution or by FEM modelling. For (A < a > M < a > B < a > N) with a =1.00 m and d = 10 mm, the error values are $F_V = 0.089$ per cent and $F_P = 0.44$ mrad, which suggests that this configuration does not lead to substantial errors in impedance magnitude and phase. For a = 0.25 m, the error values are substantially larger with $F_V =$ 0.35 per cent and $F_P = 1.77$ mrad and can no longer be neglected.

We would like to point out that the estimated maximum errors assume a vertical electrode installation. In case of an inclined electrode, the error increases due to the potentially greater distance between the two outer earth contact points of the electrode and thus the longer contact surface in the direction of the electric field. For small inclination angles α of an electrode inserted to a depth r, this increased separation can be approximated by $2\pi r\alpha/360$ (for α in degree). For a 10 mm diameter electrode installed to a depth of r = 50 mm with a small inclination angle of $\alpha = 1^{\circ}$, this approximation implies an increase of 8.7 per cent in separation. This directly translates to an increase in error by the same amount according to eq. (24) if a constant electric field is assumed. Therefore, substantially larger electrode effects and associated measurement errors can be expected even for slightly inclined electrodes.

In principle, error estimations for the effect of heterogeneous contact impedances should also consider electrode effects at the current electrodes. However, the concepts presented here cannot easily be transferred to the current electrodes because the excitation current is usually so high that non-linear effects need to be considered. The effect of heterogeneous contact impedances along the current electrodes is briefly addressed for SIP measurements in Zimmermann et al. (2008b), but should be investigated in more detail in a future study.

5 SUMMARY AND CONCLUSIONS

We presented a new model that attributes observed electrode effects to a heterogeneous distribution of contact impedance at the surface of potential electrodes. This is an alternative mechanism intended to replace the notion that observed electrode effects are merely due to the presence of metal in the electrical field. In the proposed model, the internal electric potential of a passive metal electrode located in an electric potential field is calculated. The heterogeneous contact impedances are modelled with a distributed network that describe the impedance of the electrical transition from ionic conduction to electronic conduction at the electrode surface. A simplified electrical model of a corrosion process is used for this purpose. For this arrangement, the resulting amplitudes and phase spectra of the measured electrode potential were calculated with respect to a reference point. For the ideal case with a homogeneous contact impedance, the predicted amplitude is frequency-independent and the phase is zero. For heterogeneous contact impedances, the model predicts frequency-dependent amplitudes and phases with both negative or positive phase peaks. The phase errors depend on the electrode geometry, the potential distribution around the electrode, and the distribution of the contact impedances at the electrode surface. An approximation of expected electrode effects in terms of amplitude and phase errors was obtained from the dimensions of the electrodes in relation to the electrode spacing. To avoid phase errors, the model suggests that this potential difference or the electrical field at the electrode should be small compared to the measured electrode potential. This can be achieved, for example, by keeping the electrodes as small as possible, installing the electrodes in chambers, installing the electrodes perpendicularly in relation to the electric field, or by avoiding configurations that generate an electric field at the electrode but only measure a small potential difference.

To provide experimental evidence to support the model development, laboratory SIP and EIT measurements were performed. A

first set of SIP measurements in a sample holder with a metal sphere between two non-polarizing potential electrodes showed that the mere presence of metal leads to relatively small electrode effects below 1 mrad, which was explained by the small volume fraction of the metal despite the small electrode spacing. When the same metal sphere was used as a potential electrode, observed electrode effects were approximately twice as strong and depended on the orientation of the electrode in the electric potential field. The latter observation provided strong support for the proposed model that relates electrode effects to heterogeneous contact impedances. In a second step, laboratory EIT measurements on a cylindrical sample holder were made with retracted current electrodes and retracted as well as non-retracted potential electrodes. When the retracted potential electrodes were used, the observed electrode effects due to the presence of the non-retracted electrodes was small as in the case of the SIP measurements with the metal sphere. Electrode effects were stronger when the non-retracted potential electrodes were used. More importantly, the strength of the electrode effects was found to vary considerably between different electrode configurations, and the relative strength of this variation was well described by the proposed model for electrode effects due heterogeneous contact impedances. For unfavourable electrode configurations, the observed electrode effects were as high as 40 mrad.

In a final step, implications of this new type of electrode effect for the accuracy of complex electrical resistivity measurements were analysed and discussed. For laboratory SIP and EIT measurements, close proximity of electrodes can often not be avoided, which can lead to phase errors of several mrads without additional measures. Therefore, potential electrodes should not be inserted into the applied electrical field in small-scale laboratory investigations with closely spaced electrodes. This can be achieved by retracting electrodes into their plastic electrode chambers or by the use of non-polarizing electrodes, which typically have retracted metal wires inside by design. From experiments with retracted potential electrodes presented in this study, it was concluded that a retraction by twice the diameter of the plastic electrode chamber is sufficient to remove electrode effects. For field EIT measurements, electrode separations are typically larger, which based on the presented model leads to smaller electrode effects well below 1 mrad for electrode separations of 1 m or larger and an electrode diameter of 10 mm. For an electrode separation of 0.25 m and the same electrode diameter, electrode effects were still below 1 mrad except for gamma-type electrode configurations, which should thus be avoided in EIT experiments with closely spaced electrodes.

Overall, it is concluded that the proposed model for a new type of electrode effect due to heterogeneous contact impedances was well supported by experimental results and provided useful insights in the expected range of errors for complex resistivity measurements. Correction of these electrode effects in post-processing remains elusive because of the lack of information on the distribution of the contact impedances along the electrode surface and the expected dynamic nature of the contact impedance. Therefore, efforts should be focused on avoiding electrode effects based on the presented model analysis following the provided recommendations.

ACKNOWLEDGMENTS

We wish to thank Walter Glaas for the continued support of the development of SIP and EIT measurement systems, as well as the assistance with the presented laboratory SIP and EIT measurements.

DATA AVAILABILITY

The data underlying this paper will be shared on reasonable request to the corresponding author.

REFERENCES

- Barsoukov, E. & MacDonald, J.R., 2005. *Impedance Spectroscopy—Theory, Experiment, and Applications*, 2nd edn, Wiley.
- Böcker, M., Flores Orozco, A. & Kemna, A., 2018. Electrochemical polarization around metallic particles. Part 1: the role of diffuse-layer and volume-diffusion relaxation, *Geophysics*, 83(4), E203–E217.
- Binley, A., Slater, L.D., Fukes, M. & Cassiani, G., 2005. Relationship between spectral induced polarization and hydraulic properties of saturated and unsaturated sandstone, *Water Resour. Res.*, **41**(12), doi:10.1029/2005WR004202.
- Binley, A., Keery, J., Slater, L., Barrash, W. & Cardiff, M., 2016. The hydrogeologic information in cross-borehole complex conductivity data from an unconsolidated conglomeratic sedimentary aquifer, *Geophysics*, 81(6), E409–E421.
- Börner, J.H., Herdegen, V., Repke, J.-U. & Spitzer, K., 2017. Spectral induced polarization of the three-phase system CO₂-brine-sand under reservoir conditions, *Geophys. J. Int.*, 208(1), 289–305.
- Breede, K., Kemna, A., Esser, O., Zimmermann, E., Vereecken, H. & Huisman, J.A., 2011. Joint measurement setup for determining spectral induced polarization and soil hydraulic properties, *Vadose Zone J.*, 10(2), 716–726.
- Doering, M., Kieninger, J., Urban, G.A. & Weltin, A., 2022. Electrochemical microelectrode degradation monitoring: in situ investigation of platinum corrosion at neutral pH, *J. Neural Eng.*, 19, doi:10.1088/1741-2552/ac47da
- Doetsch, J., Fiandaca, G., Auken, E., Christiansen, A.V., Cahill, A.G. & Jakobsen, R., 2015. Field-scale time-domain spectral induced polarization monitoring of geochemical changes induced by injected CO₂ in a shallow aquifer, *Geophysics*, 80(2), WA113–WA126.
- Flores Orozco, A., Williams, K.H., Long, P.E., Hubbard, S.S. & Kemna, A., 2011. Using complex resistivity imaging to infer biogeochemical processes associated with bioremediation of an uranium-contaminated aquifer, *J. geophys. Res.*, **116**, doi:10.1029/2010jg001591.
- Flores Orozco, A., Kemna, A., Oberdorster, C., Zschornack, L., Leven, C., Dietrich, P. & Weiss, H., 2012. Delineation of subsurface hydrocarbon contamination at a former hydrogenation plant using spectral induced polarization imaging, J. Contam. Hydrol., 136, 131–144.
- Gurin, G., Titov, K. & Ilyin, Y., 2019. Induced polarization of rocks containing metallic particles: evidence of passivation effect, *Geophys. Res. Lett.*, 46(2), 670–677.
- Hansen, P.C., Jensen, T.K. & Rodriguez, G., 2007. An adaptive pruning algorithm for the discrete L-curve criterion, J. Comput. Appl. Math., 198(2), 483–492.
- Huisman, J.A., Zimmermann, E., Esser, O., Haegel, F.H., Treichel, A. & Vereecken, H., 2016. Evaluation of a novel correction procedure to remove electrode impedance effects from broadband SIP measurements, *J. appl. Geophys.*, 135, 466–473.
- Izumoto, S., Huisman, J.A., Wu, Y.X. & Vereecken, H., 2020. Effect of solute concentration on the spectral induced polarization response of calcite precipitation, *Geophys. J. Int.*, 220(2), 1187–1196.
- Jöttner, K. & Lorenz, W., 1989. Electrochemical impedance spectroscopy (EIS) of corrosion processes on inhomogeneous surfaces, in *Materials Science Forum*, Vol. 44, pp. 191–204, Trans Tech Publ.
- Kelter, M., Huisman, J.A., Zimmermann, E. & Vereecken, H., 2018. Field evaluation of broadband spectral electrical imaging for soil and aquifer characterization, *J. appl. Geophys.*, 159, 484–496.
- Kemna, A., Binley, A., Ramirez, A. & Daily, W., 2000. Complex resistivity tomography for environmental applications, *Chem. Eng. J.*, 77(1–2), 11– 18.
- Kemna, A. et al., 2012. An overview of the spectral induced polarization method for near-surface applications, Near Surf. Geophys., 10(6), 453– 468.

- Leroy, P., Revil, A., Kemna, A., Cosenza, P. & Ghorbani, A., 2008. Complex conductivity of water-saturated packs of glass beads, *J. Coll. Interf. Sci.*, 321(1), 103–117.
- Levy, L. et al., 2022. Quantifying reagent spreading by cross-borehole electrical tomography to assess performance of groundwater remediation, Water Resour. Res., 58(9), doi:10.1029/2022WR032218.
- Mellage, A., Smeaton, C.M., Furman, A., Atekwana, E.A., Rezanezhad, F. & Van Cappellen, P., 2018. Linking spectral induced polarization (SIP) and subsurface microbial processes: results from sand column incubation experiments, *Environ. Sci. Technol.*, 52(4), 2081–2090.
- Olsson, P.I., Fiandaca, G., Larsen, J.J., Dahlin, T. & Auken, E., 2016. Doubling the spectrum of time-domain induced polarization by harmonic de-noising, drift correction, spike removal, tapered gating and data uncertainty estimation, *Geophys. J. Int.*, 207(2), 774–784.
- Randles, J. E.B., 1947. Kinetics of rapid electrode reactions, *Discuss. Faraday Soc.*, 1, 11–19.
- Revil, A. & Florsch, N., 2010. Determination of permeability from spectral induced polarization in granular media, *Geophys. J. Int.*, 181(3), 1480– 1498
- Revil, A., Karaoulis, M., Johnson, T. & Kemna, A., 2012. Review: Some low-frequency electrical methods for subsurface characterization and monitoring in hydrogeology, *Hydrogeol. J.*, 20(4), 617–658.
- Revil, A., Soueid Ahmed, A., Coperey, A., Ravanel, L., Sharma, R. & Panwar, N., 2020. Induced polarization as a tool to characterize shallow landslides, J. Hydrol., 589, doi:10.1016/j.jhydrol.2020.125369.
- Schmutz, M., Revil, A., Vaudelet, P., Batzle, M., Vinao, P.F. & Werkema, D.D., 2010. Influence of oil saturation upon spectral induced polarization of oil-bearing sands, *Geophys. J. Int.*, 183(1), 211–224.
- Schwartz, N. & Furman, A., 2012. Spectral induced polarization signature of soil contaminated by organic pollutant: experiment and modeling, *J. geophys. Res.*, 117(B10), doi:10.1029/2012jb009543.
- Scott, J. B.T. & Barker, R.D., 2005. Characterization of sandstone by electrical spectroscopy for stratigraphical and hydrogeological investigations, Ouart. J. Eng. Geol. Hydrogeol., 38, 143–154.
- Titov, K., Komarov, V., Tarasov, V. & Levitski, A., 2002. Theoretical and experimental study of time domain-induced polarization in water-saturated sands, *J. appl. Geophys.*, 50(4), 417–433.
- Titov, K., Kemna, A., Tarasov, A. & Vereecken, H., 2004. Induced polarization of unsaturated sands determined through time domain measurements, Vadose Zone J., 3(4), 1160–1168.
- Ulrich, C. & Slater, L.D., 2004. Induced polarization measurements on unsaturated, unconsolidated sands, *Geophysics*, 69(3), 762–771.
- Vinegar, H.J. & Waxman, M.H., 1984. Induced polarization of shaly sands, Geophysics, 49(8), 1267–1287.

- Wainwright, H.M., Orozco, A.F., Bucker, M., Dafflon, B., Chen, J., Hubbard, S.S. & Williams, K.H., 2016. Hierarchical bayesian method for mapping biogeochemical hot spots using induced polarization imaging, *Water Resour. Res.*, 52(1), 533–551.
- Wang, C. & Slater, L.D., 2019. Extending accurate spectral induced polarization measurements into the kHz range: modelling and removal of errors from interactions between the parasitic capacitive coupling and the sample holder, *Geophys. J. Int.*, 218(2), 895–912.
- Weigand, M. & Kemna, A., 2019. Imaging and functional characterization of crop root systems using spectroscopic electrical impedance measurements, *Plant Soil*, 435(1–2), 201–224.
- Weigand, M., Zimmermann, E., Michels, V., Huisman, J.A. & Kemna, A., 2022. Design and operation of a long-term monitoring system for spectral electrical impedance tomography (sEIT), *Geosci. Instrument. Methods* Data Syst., 11(2), 413–433.
- Wong, J., 1979. Electrochemical model of the induced-polarization phenomenon in disseminated sulfide ores, *Geophysics*, 44(7), 1245–1265.
- Zhang, Z.Y. & Furman, A., 2022. Statistical analysis for biogeochemical processes in a sandy column with dynamic hydrologic regimes using spectral induced polarization (SIP) and self-potential (SP), *Geophys. J. Int.*, 233(1), 564–585.
- Zimmermann, E., 2011. Phasengenaue Impedanzspektroskopie und tomographie för geophysikalische Anwendungen, *PhD thesis*, Rheinischen Friedrich-Wilhelms-Universität, Bonn, URN: urn:nbn:de:hbz:5N-24601
- Zimmermann, E., Kemna, A., Berwix, J., Glaas, W., Munch, H.M. & Huisman, J.A., 2008a. A high-accuracy impedance spectrometer for measuring sediments with low polarizability, *Meas. Sci. Technol.*, 19(10), doi:10.1088/0957-0233/19/10/105603.
- Zimmermann, E., Kemna, A., Berwix, J., Glaas, W. & Vereecken, H., 2008b.
 EIT measurement system with high phase accuracy for the imaging of spectral induced polarization properties of soils and sediments, *Meas. Sci. Technol.*, 19(9), doi:10.1088/0957-0233/19/9/094010.
- Zimmermann, E., Huisman, J.A., Kemna, A., Berwix, J., Glaas, W., Meier,
 H., Wolters, B. & Esser, O., 2010. Advanced electrical impedance tomography system with high phase accuracy, in *Proceedings of the 6th World Congress on Industrial Process Tomography (WCIPT6)*, pp. 583–591,
 Bejing, China.
- Zimmermann, E., Huisman, J.A., Mester, A. & van Waasen, S., 2019.
 Correction of phase errors due to leakage currents in wideband EIT field measurements on soil and sediments, *Meas. Sci. Technol.*, 30(8), doi:10.1088/1361-6501/ab1b09.